Volume 59
Number 30
18 April 2023
Pages 4395–4540

ChemComm

Chemical Communications

rsc.li/chemcomm

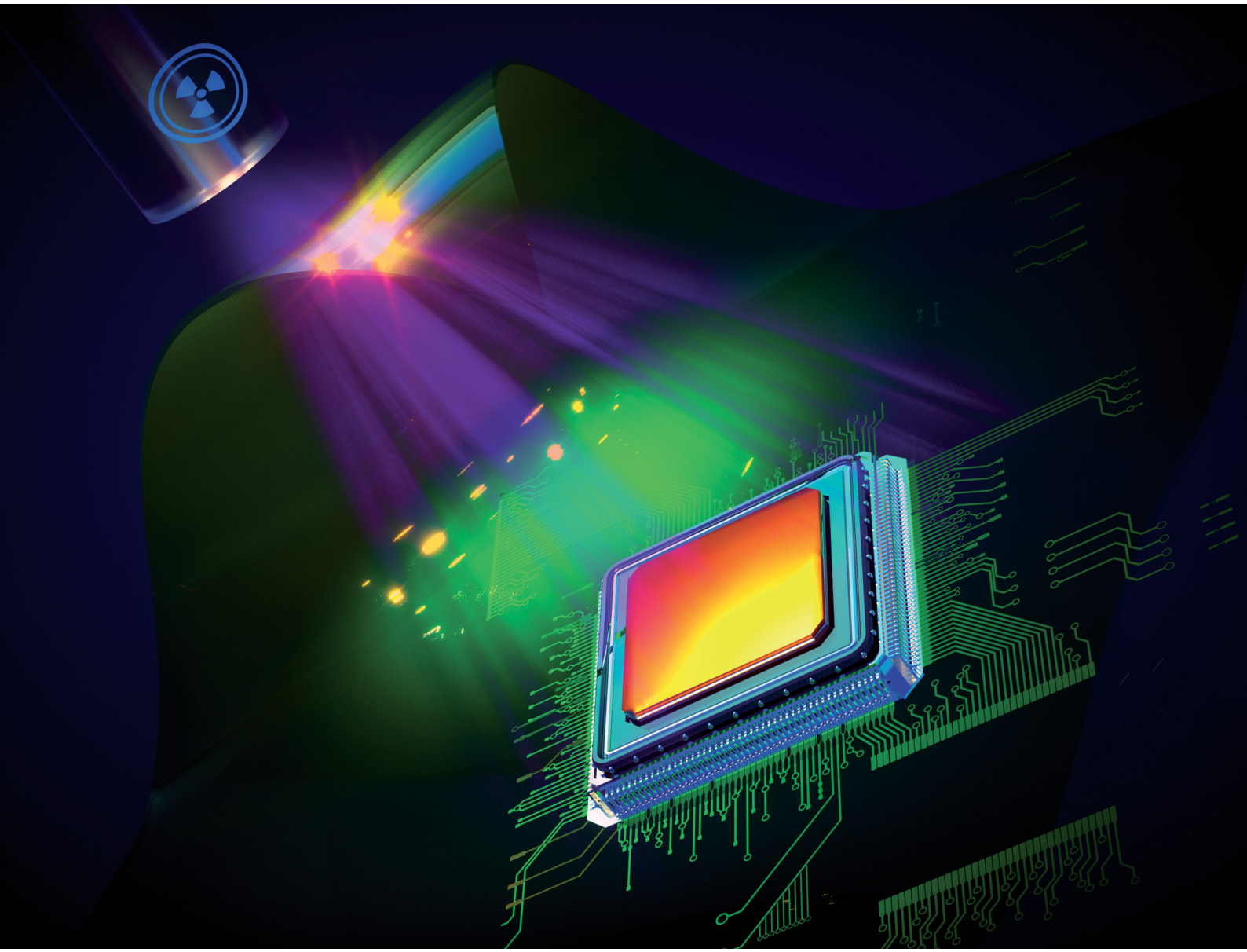

ISSN 1359-7345

ROYAL SOCIETY OF CHEMISTRY

COMMUNICATION

Omar F. Mohammed *et al.*

Zero-dimensional Cu(I)-based organometallic halide with green cluster-centred emission for high resolution X-ray imaging screens

ChemComm

COMMUNICATION

View Article Online
View Journal | View Issue

Cite this: *Chem. Commun.*, 2023, 59, 4447

Received 16th February 2023,
Accepted 14th March 2023

DOI: 10.1039/d3cc00730h

rsc.li/chemcomm

Zero-dimensional Cu(I)-based organometallic halide with green cluster-centred emission for high resolution X-ray imaging screens†

Alaa M. Almushaikeh,[a] Hong Wang,[ab] Luis Gutiérrez-Arzaluz,[a] Jun Yin,[c] Ren-Wu Huang,[b] Osman M. Bakr[b] and Omar F. Mohammed*[ab]

In this communication, we report a low-dimensional perovskite-related structure based on Cu(I) organometallic halide with strong green cluster-centred emission and near-unity photoluminescence quantum yield. The 0D $[Rb(18\text{-crown-6})]_2Cu_4I_6$ was sucessfully applied for X-ray imaging screens which exhibit high spatial resolution of 16.8 lp mm^{-1} and low detection limit of 458 nGy s^{-1}.

Lead-free perovskites and their related structures have received tremendous attention in recent years for their prodigious optoelectronics properties.[1,2] In particular, metal halide materials based on Cu(I) are considered a promising class of materials due to their low toxicity compared with lead, facile solution-based synthesis and fabrication, low cost, and copper abundance compared with rare-earth elements and noble materials; these characteristics make the materials ideal for various applications.[3–5] In addition, the structural and optical properties of Cu(I)-based complexes are diverse and can be altered by varying the organic component, the reaction conditions, or the structural dimensionality of the complexes.[4,6] Among various Cu(I) structures, low-dimensional Cu(I) complexes and clusters exhibit promising characteristics, which are attributed to their perovskite-related structures. These materials feature a polyhedral metallic component surrounded by an organic component, resulting in a highly stable chemical structure with high photoluminescence properties and low light scattering due to the quantum confinement effect.[4,6,7]

X-ray imaging has attracted the attention of researchers recently due to its modern, everyday life applications.[2] Through scintillators, X-ray photons are converted into visible or near-IR light for imaging and detection purposes.[1] Present-day commercialized scintillators are based on bulk crystals such as thallium-doped cesium iodide (CsI:Tl), cerium-doped lanthanum bromide ($LaBr_3$:Ce), and terbium-doped gadolinium oxysulfide (Gd_2O_2S:Tb).[8–10] These scintillators exhibit high light yields, but they are inherently fragile, brittle and limited by their high cost and tiring fabrication process, which limits their utilization in many applications.[1,11] Consequently, developing scintillators with a low detection limit, high light yield, low fabrication cost, facile scalability, and high resolution is crucial.[5] Recently, Cu(I) complexes have emerged as excellent candidates for X-ray imaging scintillators due to their facile synthesis process, excellent photoluminescence properties, high stability, low cost, and high atomic number.[3,6]

Herein, we introduce a 0D Cu(I)-based organometallic halide with a crown ether as the organic component, which is coordinated with Rb^+. The compound $[Rb(18\text{-crown-6})]_2Cu_4I_6$·acetone consists of $[Cu_4I_6]^{2-}$ clusters isolated by the organic part facilitating an enhanced PL performance to occur. Subsequently, the optical properties of the material were thoroughly explored and characterized, where an asymmetric green broadband emission centred at 527 nm with near-unity PLQY was observed. Optical properties measurements, along with density functional theory (DFT) calculations, revealed that the source of emission is the cluster centres (CC), which generate the broadband green emission upon UV or X-ray excitation (Fig. 1a). The outstanding optical properties of the material, along with the high atomic number of Cu, I, and Rb, motivated further investigation of the material's radioluminescence properties under X-ray irradiation, as well as its performance as an X-ray imaging screen.

The structure of an as-grown RCCI single crystal was determined by single-crystal X-ray diffraction (SCXRD) (Fig. S1, ESI†). Fig. 1b shows the crystal structure of $[Rb(18\text{-crown-6})]_2Cu_4I_6$·

[a] *Advanced Membranes and Porous Materials Center, Division of Physical Science and Engineering, King Abdullah University of Science and Technology, Thuwal 23955-6900, Kingdom of Saudi Arabia. E-mail: Omar.Abdelsaboor@kaust.edu.sa*
[b] *KAUST Catalysis Center, Division of Physical Sciences and Engineering, King Abdullah University of Science and Technology, Thuwal 23955-6900, Kingdom of Saudi Arabia*
[c] *Department of Applied Physics, The Hong Kong Polytechnic University, Kowloon, 999077, Hong Kong, P. R. China*

† Electronic supplementary information (ESI) available: Experimental section (Section S1); Supplemental Figures and Tables (Section S2) and CIF file (Section S3). CCDC 2237940. For ESI and crystallographic data in CIF or other electronic format see DOI: https://doi.org/10.1039/d3cc00730h

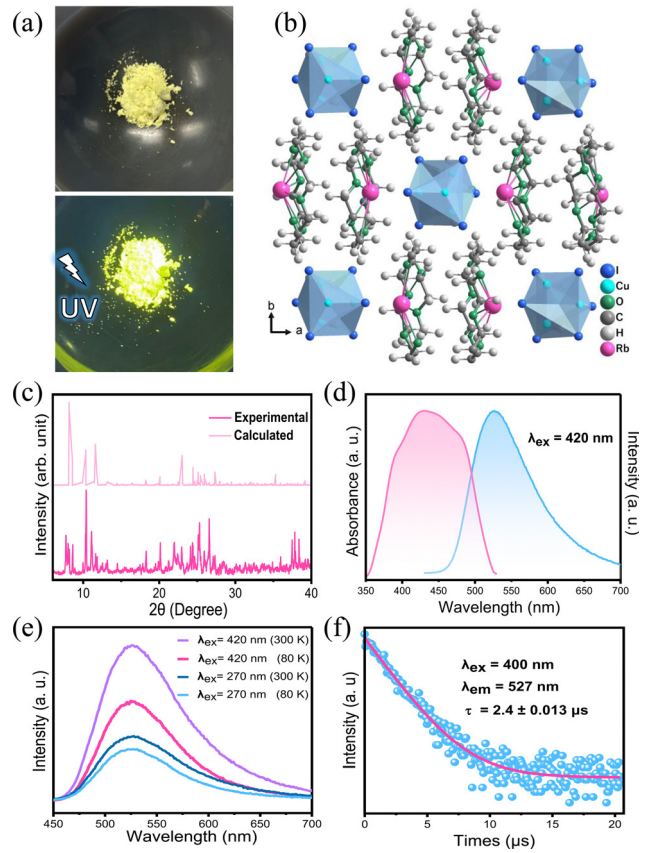

Fig. 1 (a) Images of RCCI powder under ambient light and UV irradiation (365 nm). (b) Crystal structure of $[Rb(18\text{-crown-}6)]_2Cu_4I_6$·acetone, acetone is omitted for clarity. (c) PXRD pattern of RCCI·acetone. (d) Absorption and emission spectra of RCCI imaging screens. (e) Emission spectra of RCCI imaging screens at different excitation wavelengths (270 and 420 nm) and different temperatures (80 and 300 K). (f) Emission decay curves of RCCI imaging screens.

acetone, which belongs to the orthorhombic space group *Pnma*. The main crystallographic structure parameters are presented in Table S1 (ESI†), and the crystallographic information file (CIF) of single-crystal RCCI·acetone is provided in the ESI.† Rather easily, 18-crown-6 binds alkali metal ions into its central cavity to form complexes that can be crystallized.[12,13] The 0D RCCI single crystal consists of Rb^+ coordinated with 18-crown-6 to form $[Rb(18\text{-crown-}6)]^+$ complex cations and $[Cu4I6]^{2-}$ polymeric anions. The latter consists of Cu^+ ions coordinated by three I^- ions forming CuI_3 triangles, which are connected by edges and nodes and disordered over eight positions. Each $[Cu_4I_6]^{2-}$ is isolated from the nearest cluster by two $[Rb(18\text{-crown-}6)]^+$ cations.[14] The distance between the centres of two adjacent $[Cu_4I_6]^{2-}$ clusters is 12.55 Å. Notably, the Cu–I bond distances are in the range of 2.57–2.60 Å, while the range of Cu–Cu bond distances is 2.609–2.695 Å. Because the Cu–Cu bond in $[Cu_4I_6]^{2-}$ clusters is shorter than the sum of the van der Waals radii of Cu(I) (3.84 Å), this entails a strong metal–metal bonding interaction in the cluster.[3] This interaction, which results from the closed-shell d^{10}–d^{10} Cu^I–Cu^I interactions, plays a major role in determining the photophysical properties of ligand-stabilized Cu(I)-based complexes.[3,6] Acetone molecules are trapped during the crystallization process and fill out the voids within the crystal structure. The powder X-ray diffraction (PXRD) pattern of ground $[Rb(18\text{-crown-}6)]_2Cu_4I_6$·acetone crystals is shown in Fig. 1c, which is almost consistent with the simulated PXRD pattern obtained from single-crystal structure data for RCCI·acetone, slight variations might be attributed to the escape of acetone molecule from the crystal structure. Pure $[Rb(18\text{-crown-}6)]_2Cu_4I_6$ (RCCI) microcrystalline powder was also successfully synthesized by direct reaction of the precursors (ESI†). Although the microcrystalline powder is inadequate for single-crystal structure analysis, it is suitable for preparing imaging screens, and it also represents a more environmentally friendly synthesis approach to obtain the compound because it does not require the use of any additional chemical solvents. The morphology of RCCI microcrystalline powder was investigated by SEM. The SEM image shown in Fig. S2 (ESI†) reveals the agglomeration of multitudinous nanoparticles. The EDX spectrum shows the distribution of Cu, I, and Rb, which were disseminated homogeneously throughout the powder (Fig. S3, ESI†). The thermostability of the material was investigated by thermogravimetric analysis (TGA), which indicates good thermostability with no obvious degradation up to 200 °C (Fig. S4, ESI†).

Both the high-quality RCCI crystals and microcrystalline powder emit intense green light visible to the naked eye upon UV irradiation (Fig. 1a and Fig. S1, ESI†). The photophysical properties of the compound were further investigated. The photoluminescence quantum yield of the green emission of the RCCI was calculated to be near unity (93.4%). The PL and absorption spectra of RCCI at room temperature are shown in Fig. 1d, revealing a broadband absorption peak with a range of 300–500 nm, which can be seen in similar Cu(I) metal halides.[7,14–16] The PL spectrum with an excitation wavelength of 420 nm demonstrates broadband emission centred at 527 nm. Note that the emission spectra obtained at different wavelengths (270 and 420 nm) and different temperatures (80 and 300 K) are almost identical (Fig. 1e). Moreover, the PL emission was investigated at different temperatures, and the emission peak position remained consistent although the spectrum became narrower due to the decrease in the population of thermally filled vibrational states, which occurs at lower temperatures (Fig. S5, ESI†).[17] Additionally, the normalized PL emission at different excitation wavelengths remained invariant (Fig. S6, ESI†). The time-resolved photoluminescence at room temperature shows a long lifetime of 2.4 μs through mono-exponentially fitting (Fig. 1f). To understand the electronic properties of the RCCI·acetone single crystal, we carried out DFT calculations. The calculated direct band gap (2.01 eV) is slightly smaller than the experimental value (2.3 eV) derived from the Tauc equation (Fig. 2a and Fig. S7, ESI†), which is attributed to the well-known self-interaction error raised by the GGA/PBE function. The projected density of states (PDOS) show that the valence band maximum (VBM) mostly consists of Cu-3d and I-5p states, while the conduction band minimum (CBM) is dominated by I-5p states (Fig. 2b). As shown in Fig. 2c, the electronic charge densities further indicate that the VBM and

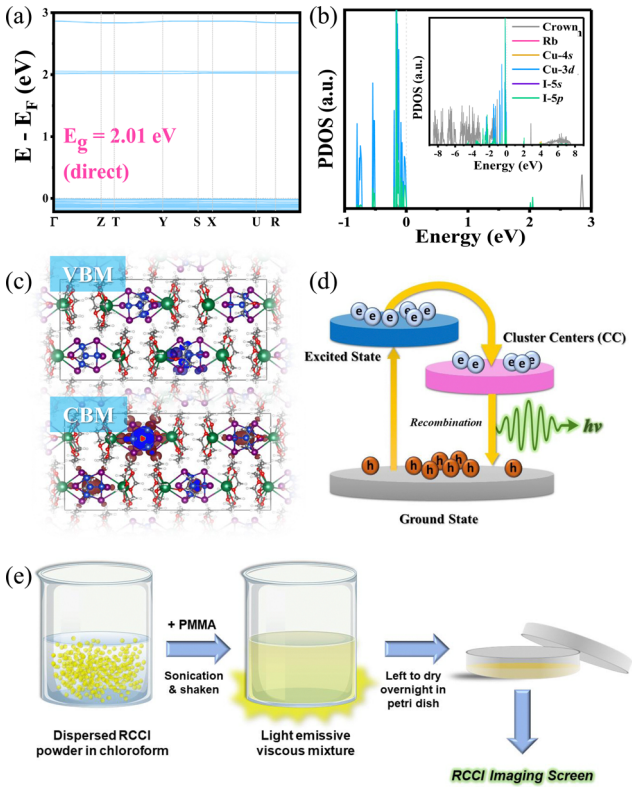

Fig. 2 (a) Electronic band gap structure. (b) PDOS of RCCI; the inset shows a PDOS with a larger range. (c) Plots of wavefunction $|\Psi|^2$ of the CBM and VBM. (d) Schematic diagram of the photophysical processes. (e) Schematic illustration of the preparation procedure of RCCI@PMMA imaging screens.

CBM are localized in $[Cu_4I_6]^{2-}$, suggesting that organic components would not contribute to the optical response of the RCCI acetone single crystal. Hence, the role of the organic part in this compound is simply to isolate the Cu(I)-based clusters, allowing for favourable PL performance to occur.[3]

Considering the afreomentioned results, we propose a configuration coordinate diagram describing the photophysical processes that occur in 0D RCCI (Fig. 2d). Upon UV excitation, the electrons of $[Cu_4I_6]^{2-}$ are excited from the ground state to the excited states, forming free excitons (FEs) in the sub-picosecond range as indicated by the transient absorption (TA) measurements shown in Fig. S8 (ESI†). The FEs relax into the cluster-centred (CC) excited states, which move further back down to the ground state by emitting an intense green emission. This optical response is similar to the self-trapped exciton (STE) emission observed in low-dimensional perovskites.[7] The photophysical properties of RCCI and its high atomic number indicate that RCCI is a promising candidate for X-ray imaging screens.

We investigated the X-ray imaging performance of 50 wt% RCCI@PMMA imaging screens with respect to X-ray absorption, radioluminescence spectrum, detection limit, stability, and image resolution. Notably, the facile preparation process shown in Fig. 2e permits a prompt optimization process of the imaging screens (ESI†). The X-ray absorption of RCCI was examined using the NIST Standard Reference Database with photon energies ranging from 1 to 100 keV (Fig. 3a).[18] RCCI exhibits an absorption coefficient comparable with that of commercial scintillators such as BGO ($Bi_4Ge_3O_{12}$). This is attributed to the high atomic numbers of I, Rb, and Cu. Furthermore, we evaluated the RL spectra of RCCI imaging screens under a dose rate of 4.53 mGy s^{-1}, as shown in Fig. 3b. The RL spectra are indistinguishable from the PL spectra, implying that the radiative recombination pathway is similar

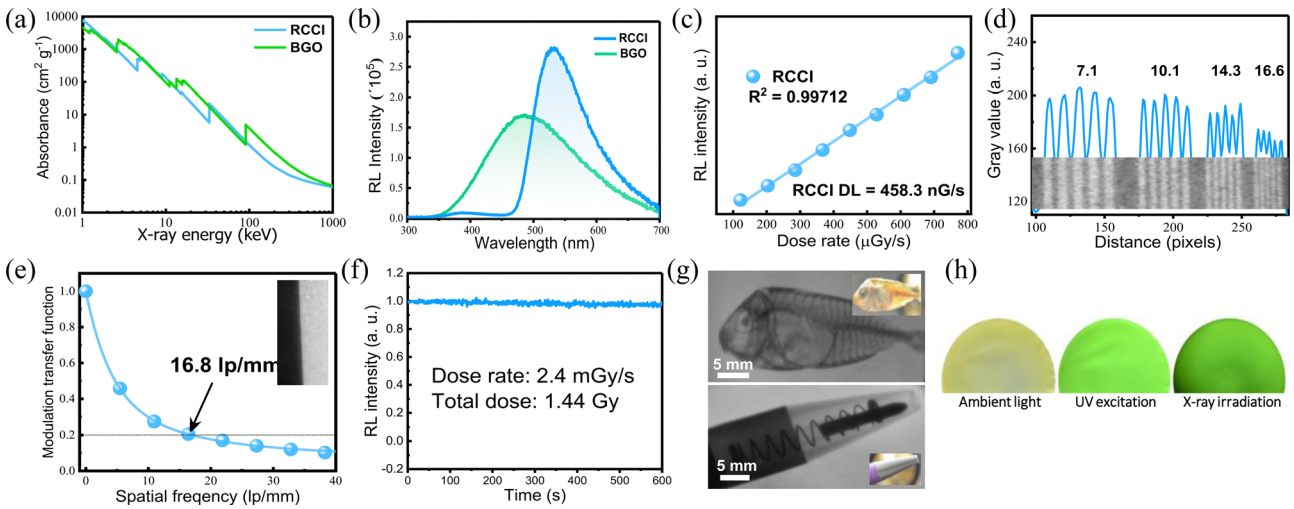

Fig. 3 X-ray performance of RCCI@PMMA imaging screens. (a) Absorption coefficients of RCCI and BGO as a function of photon energy. (b) RL spectra of RCCI@PMMA imaging screens and BGO under X-ray irradiation with a dose rate of 4.53 mGy s^{-1}. (c) RL intensity of RCCI@PMMA imaging screens *versus* the X-ray dose rate and the detection limit. (d) X-ray line bar profile obtained using the X-ray image of standard lead bar phantoms (inset); numbers (7.1–16.6) refer to lp mm^{-1}. (e) The MTF plot of the RCCI@PMMA imaging screen and the measured resolution; inset shows the edge of the X-ray image used for MTF calculation. (f) RL intensity of RCCI@PMMA as a function of time. (g) X-ray images of a ballpoint pen and a dried fish. The insets represent the images under ambient light. (h) Images of RCCI@PMMA imaging screen under ambient light, UV irradiation (365 nm), and X-ray irradiation (50 kV). All X-ray images were recorded at 50 kV.

for both UV and X-ray irradiation. A standard BGO sample with a light yield of 10 000 photons MeV^{-1} was used to help assess the light yield of RCCI imaging screens, as both the sample and BGO have a similar RL spectra range and X-ray attenuation coefficients. The light yield was found to be 10 600 photons MeV^{-1}. To estimate the detection limit, we measured the RL spectra as a function of the X-ray dose rate. The integrated RL intensity depends linearly on the X-ray dose rate, which is a requirement for X-ray imaging applications. The detection limit was found to be 458 nGy s^{-1}, for a signal-to-noise ratio of 3, which is approximately 10 times lower than the dose required for typical medical diagnostics (5.5 μGy s^{-1}) (Fig. 3c).[19]

We further investigated the X-ray imaging performance of 50 wt% RCCI@PMMA screens. The spatial resolution of RCCI@PMMA was examined by using standard X-ray lead bar phantoms, and was found to be 16.6 lp mm^{-1} (Fig. 3d). Additionally, the modulation transfer function (MTF), derived using an image of a slanted edge, indicated an ultrahigh resolution of 16.8 lp mm^{-1} at MTF = 0.2, which is consistent with the resolution obtained using the standard line-pair bar, as shown in Fig. 3e. The spatial resolution of RCCI is high compared with other scintillators such as commercial CsI(Tl) (10 lp mm^{-1}), as well as recently reported organometallic Cu(I) X-ray screens $(DIET)_3Cu_3Br_3$ (11.71 lp mm^{-1}) and $(C_8H_{20}N)_2Cu_2Br_4$ (9.54 lp mm^{-1}).[20–22] Additionally, RCCI displayed strong RL emission stability, withstanding a dose rate of 2.4 mGy s^{-1} for more than 10 min, with the RL of the sample remaining over 97.6% of its initial value, as shown in Fig. 3f. The total exposure dose was approximately 1.44 Gy, which is comparable to more than 14 400 chest radiograph doses in which each patient is exposed to 0.1 mGy during the imaging procedure.[23]

Herewith, we performed imaging of different objects under X-ray irradiation using a homemade X-ray imaging setup, shown in Fig. S9 (ESI†). Initially, we demonstrated that RCCI can be used to image a ballpoint pen with a metal spring inside it, clearly showing the details of the internal parts (the plastic tip, metallic spring, and aluminium barrel). Additionally, we imaged a biological target, a small, dried fish. The image shows the features of its internal structure (spine, skull, and dorsal fin) (Fig. 3g). X-ray images of a shadow mask and a CPU card are shown in Fig. S10 (ESI†). Additionally, we show images of a single RCCI imaging screen under ambient light, UV excitation, and X-ray irradiation (Fig. 3h). The results illustrate that RCCI is an auspicious material for next-generation X-ray imaging applications.

In summary, we report a 0D Cu(I) organometallic halide (RCCI) with an intense green emission centred at 527 nm. The emission was proved experimentally and theoretically to result from the cluster-centred (CC) excited states. The as-prepared 50 wt% RCCI@PMMA imaging screens showed great potential for X-ray imaging applications, with an ultrahigh imaging resolution of up to 16.8 lp mm^{-1}. This work offers a design roadmap for the development of new low-dimensional Cu(I) luminescent materials for high-performance and flexible X-ray imaging scintillators.

The authors acknowledge funding support from KAUST. The authors acknowledge the use of KAUST Core Labs and KAUST Solar Center facilities.

Conflicts of interest

There are no conflicts to declare.

Notes and references

1 J.-X. Wang, O. M. Bakr and O. F. Mohammed, *Matter*, 2022, **5**, 2547–2549.
2 Y. Zhou, J. Chen, O. M. Bakr and O. F. Mohammed, *ACS Energy Lett.*, 2021, **6**, 739–768.
3 E. Cariati, E. Lucenti, C. Botta, U. Giovanella, D. Marinotto and S. Righetto, *Coord. Chem. Rev.*, 2016, **306**, 566–614.
4 A. Mensah, J. J. Shao, J. L. Ni, G. J. Li, F. M. Wang and L. Z. Chen, *Front. Chem.*, 2021, **9**, 816363.
5 T. He, Y. Zhou, X. Wang, J. Yin, L. Gutiérrez-Arzaluz, J.-X. Wang, Y. Zhang, O. M. Bakr and O. F. Mohammed, *ACS Energy Lett.*, 2022, **7**, 2753–2760.
6 R. Peng, M. Li and D. Li, *Coord. Chem. Rev.*, 2010, **254**, 1–18.
7 S. Li, J. Xu, Z. Li, Z. Zeng, W. Li, M. Cui, C. Qin and Y. Du, *Chem. Mater.*, 2020, **32**, 6525–6531.
8 E. V. D. van Loef, P. Dorenbos, C. W. E. van Eijk, K. Krämer and H. U. Güdel, *Appl. Phys. Lett.*, 2001, **79**, 1573–1575.
9 C. W. E. van Eijk, *Phys. Med. Biol.*, 2002, **47**, R85–R106.
10 P. Schotanus and R. Kamermans, *IEEE Trans. Nucl. Sci.*, 1990, **37**, 177–182.
11 Y. Zhang, R. Sun, X. Ou, K. Fu, Q. Chen, Y. Ding, L. J. Xu, L. Liu, Y. Han, A. V. Malko, X. Liu, H. Yang, O. M. Bakr, H. Liu and O. F. Mohammed, *ACS Nano*, 2019, **13**, 2520–2525.
12 E. Merzlyakova, S. Wolf, S. Lebedkin, L. Bayarjargal, B. L. Neumeier, D. Bartenbach, C. Holzer, W. Klopper, B. Winkler, M. Kappes and C. Feldmann, *J. Am. Chem. Soc.*, 2021, **143**, 798–804.
13 J. A. Rusanova, K. V. Domasevitch, O. Y. Vassilyeva, V. N. Kokozay, E. B. Rusanov, S. G. Nedelko, O. V. Chukova, B. Ahrens and P. R. Raithby, *Dalton Trans.*, 2000, 2175–2182.
14 J. Huang, B. Su, E. Song, M. S. Molokeev and Z. Xia, *Chem. Mater.*, 2021, **33**, 4382–4389.
15 X. Liu, Y. Li, L. Zhou, M. Li, Y. Zhou and R. He, *Adv. Opt. Mater.*, 2022, **10**, 2200944.
16 M. Chen, C. Ye, C. Dai, R. Qi, H. Fu, C. Luo, H. Peng and H. Lin, *Adv. Opt. Mater.*, 2022, **10**, 2200278.
17 C. Zhou, H. Lin, M. Worku, J. Neu, Y. Zhou, Y. Tian, S. Lee, P. Djurovich, T. Siegrist and B. Ma, *J. Am. Chem. Soc.*, 2018, **140**, 13181–13184.
18 M. J. Berger and J. H. Hubbell, Oak Ridge, TN, 1987.
19 H. Wei, Y. Fang, P. Mulligan, W. Chuirazzi, H.-H. Fang, C. Wang, B. R. Ecker, Y. Gao, M. A. Loi, L. Cao and J. Huang, *Nat. Photon.*, 2016, **10**, 333–339.
20 X. Ou, X. Qin, B. Huang, J. Zan, Q. Wu, Z. Hong, L. Xie, H. Bian, Z. Yi, X. Chen, Y. Wu, X. Song, J. Li, Q. Chen, H. Yang and X. Liu, *Nature*, 2021, **590**, 410–415.
21 K. Han, J. Jin, B. Su, J. Qiao and Z. Xia, *Adv. Opt. Mater.*, 2022, **10**, 2200865.
22 B. Su, J. Jin, K. Han and Z. Xia, *Adv. Funct. Mater.*, 2023, **33**, 2210735.
23 S. Tie, W. Zhao, D. Xin, M. Zhang, J. Long, Q. Chen, X. Zheng, J. Zhu and W. H. Zhang, *Adv. Mater.*, 2020, **32**, e2001981.

